



# Time-dependent mechanical response of a composite PFSA membrane

Narinder S. Khattri<sup>a</sup>, Zongwen Lu<sup>a</sup>, Anette M. Karlsson<sup>a,\*</sup>, Michael H. Santare<sup>a</sup>, F. Colin Busby<sup>b</sup>, Thomas Schmiedel<sup>b</sup>

<sup>a</sup> Department of Mechanical Engineering, University of Delaware, DE 19716, USA

<sup>b</sup> Gore Fuel Cell Technologies, Elkton, MD 21922, USA

## HIGHLIGHTS

- Time-dependent mechanical behavior of reinforced PFSA characterized via experiments.
- Mechanical response of a composite membrane is investigated numerically.
- Effect of humidity cycling, thickness, and clamping pressure is studied.
- Anode side reinforced configuration develops lowest membrane stresses.

## ARTICLE INFO

### Article history:

Received 23 August 2012

Received in revised form

14 November 2012

Accepted 27 November 2012

Available online 1 December 2012

### Keywords:

Proton exchange membrane (PEM) fuel cells

Viscoelastic-plastic

Time-dependent

Composite PFSA membrane

Reinforced membrane

## ABSTRACT

The mechanical response of a composite fuel cell membrane, made from layers of reinforced and unreinforced PFSA material, is investigated via both experimental and numerical means. First, the time-dependent mechanical properties for the reinforced layers are measured for a range of environmental and loading conditions. A three-network, viscoelastic-plastic constitutive model is developed to characterize the mechanical response of this reinforced membrane material. This constitutive model is then used in finite element simulations of a fuel cell unit (consisting of composite membrane, electrodes, gas diffusion layer and bipolar plates) where the effect of relative humidity (RH) cycling on the stress response of the composite membrane is investigated. Using numerical simulations, various layering configurations for the composite membrane and different load cases are studied. The investigation provides insight into the stress response of the membrane and suggests possible configurations that may improve the effective membrane life.

© 2012 Elsevier B.V. All rights reserved.

## 1. Introduction

The goal of increasing the durability and lifetime of polymer membrane fuel cells has motivated active research and development into altering the thermal and mechanical properties of perfluorosulphonic acid (PFSA) membranes [1–5]. Specifically, to increase the mechanical strength of PFSA membranes, various reinforcing agents have been used such as polyvinylidene fluoride, expanded polytetrafluoroethylene (e-PTFE) fibrils and other polymers [6–13].

Several studies have shown an increase in the durability of membranes with the addition of e-PTFE reinforcement [14–18]. Cleghorn et al. [14] conducted single-cell life-tests with a commercial e-PTFE reinforced GORE-SELECT<sup>®</sup>1 series membrane

and reported a low rate of performance degradation under continuous H<sub>2</sub>/air operating conditions. Tang et al. [15] carried out a study comparing Nafion<sup>®</sup>2 membrane and e-PTFE reinforced PFSA membranes, and showed that the swelling and shrinkage stresses caused by water uptake are lower in the reinforced membrane and concluded that this was instrumental in their improved durability.

Viscoelastic models have been used to characterize the time-dependent mechanical properties of reinforced GORE-SELECT<sup>®</sup>-57 membranes over a wide range of temperatures and humidities [16,17]. These studies, along with another [18] that considered fatigue and creep effects, showed that the GORE-SELECT<sup>®</sup> membranes have considerably longer lifetimes due to the e-PTFE reinforcement.

Typically, membrane failure in fuel cells is defined as a critical volumetric rate of gas crossover from the anode side to the cathode side of the membrane. High compressive and residual tensile stresses developed in the membrane under hygrothermal cycling

\* Corresponding author. Present address: 2121 Euclid Avenue, SH104, Cleveland OH 44115-2214, USA. Tel.: +1 216 687 2558; fax: +1 216 687 9280.

E-mail addresses: [a.karlsson@csuohio.edu](mailto:a.karlsson@csuohio.edu), [karlsson@udel.edu](mailto:karlsson@udel.edu) (A.M. Karlsson).

<sup>1</sup> GORE-SELECT is the registered trademark of W. L. Gore & Associates, Inc.

<sup>2</sup> Nafion is the registered trademark of E.I. du Pont de Nemours & Co., Inc.

during fuel cell operation are thought to be responsible for causing fatigue loading [19–25]. This, in turn is associated with propagation of cracks and pinholes across the membrane-electrode assembly (MEA), which lead to failure [20,26]. Chemical degradation also plays a prominent role in the failure process. In order to investigate mechanical-only failures, accelerated mechanical degradation test protocols have been developed. These protocols typically involve cycling the membrane between high and low RH conditions at elevated temperatures, in an open-circuit to eliminate electro-chemical effects, while monitoring the leakage of gas across the membrane [27–30]. Gittleman et al. [26] showed experimentally that after several thousand such RH cycles, unreinforced PFSA membranes developed through-cracks in the membrane thickness direction. However, in reinforced membrane samples, the cracks were arrested by the reinforcement layer. Liu et al. [31] reported that the reinforcement of PFSA membrane with PTFE improves the dimensional stability and reduces the in-plane swelling stress in the membrane. The current study aims to increase our understanding of the mechanical behavior of the e-PTFE reinforced PFSA membrane material and the failure processes for a composite membrane consisting of two or more material layers of unreinforced PFSA (Nafion®211) and e-PTFE reinforced PFSA.

In previous work [32–34], we characterized the time, temperature and hydration dependent properties of Nafion®211 membrane and simulated its mechanical response under hygrothermal cycling in a fuel cell unit. The simulation results suggested that large (9 to 10 MPa) residual tensile stresses develop upon dehydration, which can lead to damage in the membrane. In this work, we explore the effect of the e-PTFE reinforcement on the membrane's mechanical response by simulating (via finite element simulations), a composite membrane (consisting of layers of unreinforced and reinforced membrane material) under hygrothermal conditions in a fuel cell unit assembly. We use the time-dependent properties of Nafion® membrane, presented in earlier work [32] along with the properties for the reinforced membrane material established in this work.

The description of the test setup and the experimental results pertaining to the e-PTFE reinforcement material are provided in Sections 2.1 and 2.2, respectively. A three-network viscoelastic-plastic constitutive model used to characterize the mechanical response is discussed in Section 2.3. Using the results from Section 2.3, the constitutive model is then incorporated in numerical analysis of a composite membrane in a fuel cell operating under hygrothermal loading in Section 3. Finally, the finite element simulation results for various configurations of the composite membrane are presented in Section 4. The in-plane stresses in the membrane, which have been shown to be related to crack initiation [24,35] and further degradation of the membrane, are reported for selected conditions. The effects of symmetric RH cycling (equal application from the cathode and the anode sides), asymmetric RH cycling, membrane thickness and clamping pressure are discussed for various layering configurations of the composite membrane.

## 2. Mechanical properties of the reinforced membrane material

### 2.1. Test setup

We evaluated the time-dependent mechanical properties for an e-PTFE reinforced PFSA, manufactured specifically for this study and provided by W. L. Gore & Associates Inc. The membranes are manufactured in sheets of 7  $\mu\text{m}$  nominal thickness, and the reinforcement is uniformly distributed throughout the thickness of the membrane. The reinforced membrane material has two distinct

in-plane directions designated “machine” and “transverse”. Therefore, we cut 100 mm by 30 mm rectangular test specimens from the membrane sheet in both these directions.

The test protocol is similar to that used in our previous work [33,36], but repeated here for clarity. We conducted the tests using the test setup shown in Fig. 1 consisting of an MTS Alliance™ RT/5 material testing system fitted with an ESPEC custom-designed environmental chamber. Uniaxial tensile and stress–relaxation tests were conducted under controlled environmental conditions and at selected load parameters such as displacement rates and hold strains.

Each specimen was aligned with the MTS machine axis and clamped in a pair of vise-action grips to provide a nominal gauge length of 50 mm as determined by the grip separation (Fig. 1). To achieve the desired environmental conditions in the chamber, the temperature was first set to the desired value and allowed to stabilize and then the humidity was slowly increased (or decreased) to the desired RH value with the specimen slack. Both the temperature and humidity were kept at the desired conditions for

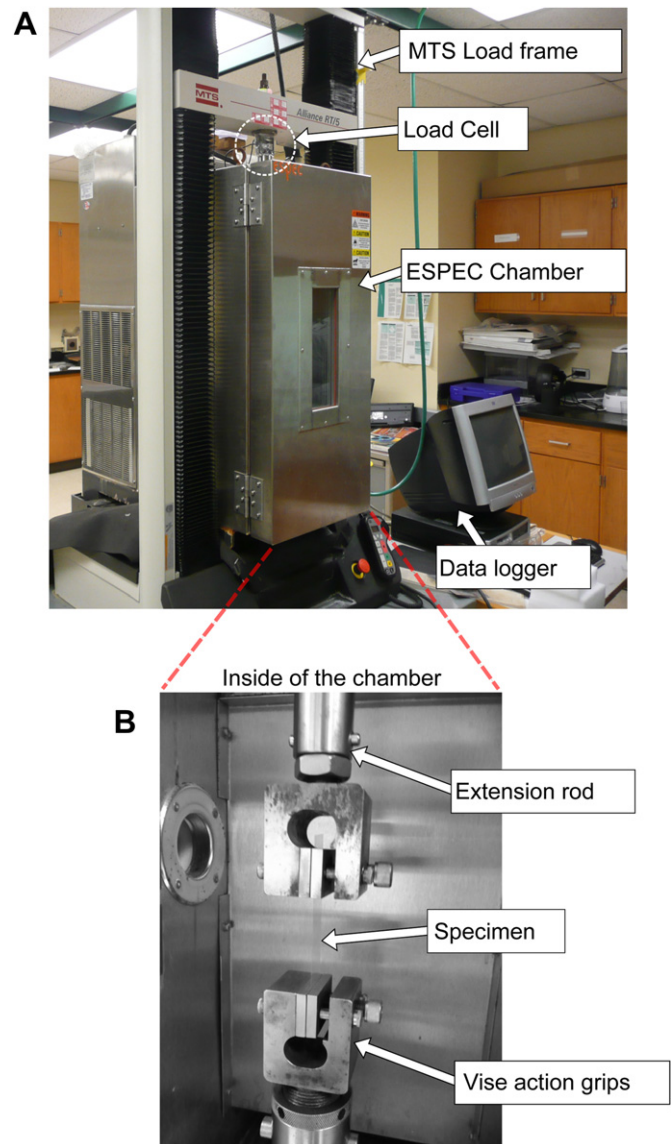


**Fig. 1.** (A) MTS alliance RT/5 material testing system with custom-designed environmental chamber from ESPEC Inc., and (B) inside of the chamber showing the specimen held with a pair of vise-action grips.

at least a half hour to ensure equilibrium conditions before applying tension. During this process, the length of the specimen changes due to the thermal and swelling deformations of the membrane. Therefore, before applying a force, the crosshead was manually adjusted until the initial force applied to the specimen was brought to a small, finite tensile value ( $\sim 0.01$  N), eliminating the initial slack caused by thermal and swelling expansions. To determine the subsequent strain, we took the undeformed length of the specimen as the original length at ambient conditions, plus the total displacement of the crosshead corresponding to the change in length caused by the change in environmental conditions.

We tested three specimens each in the machine and transverse directions at each temperature, humidity and tensile loading rate or relaxation holding strain combination. For each specimen, the pre-test thickness and width were measured with a micrometer and a caliper, respectively, at three locations along the sample before testing. The averages of these three measurements were used as the nominal dimensions of the sample under ambient conditions.

## 2.2. Experimental results

### 2.2.1. Uniaxial tensile test

From the first several sets of tests, we found the mechanical response of the reinforced membrane to be almost independent of the humidity (Fig. 2A). Therefore, the remaining tests were conducted at four temperatures (25, 45, 65 and 80 °C) and a relative humidity of 30%. Two displacement rates of 10 mm min<sup>-1</sup> and 250 mm min<sup>-1</sup> were selected, for each of the two loading directions (machine and transverse), giving 16 distinct conditions. Three specimens were tested at each condition and the average response is reported. The acquired test data, in the form of load as a function of displacement, are converted into true-stress as a function of true-strain and presented in Fig. 2A–C for selected conditions.

We make the following observations from the test results. An increase in load rate results in an increase in the elastic modulus and the proportional limit stress (Fig. 2B). There is also an observable increase in the hardening modulus with an increase in load rate (this behavior was not seen for unreinforced Nafion® membranes [32,33]). The elastic modulus and the proportional limit stress were found to decrease with an increase in temperature (Fig. 2C). However, the rate of change is reduced as the temperature is increased (80 °C). The elastic modulus, proportional limit stress and the hardening modulus (post-proportional limit tangent modulus) for various environmental and loading conditions are summarized in Fig. 3.

### 2.2.2. Stress–relaxation test

As observed for the tensile test, there was negligible effect of humidity on the relaxation response (Fig. 4A). Therefore we conducted the stress–relaxation tests at the temperatures of 25, 45, 65 and 80 °C and a humidity of 30%RH. An initial displacement rate of 10 mm min<sup>-1</sup> was used to reach the desired strain. We recorded the stress evolution of the membrane for three holding strain levels (0.05, 0.1 and 0.2) for each of the two directions of loading, giving 24 test conditions.

The results show that when the samples are held at a higher constant strain, the stress equilibrates at higher magnitude (Fig. 4B) and that the overall stress levels and the equilibrium stress decrease with an increase in temperature (Fig. 4C).

## 2.3. Constitutive model for the reinforced membrane material

Here, we present the constitutive model used to capture the time-dependent mechanical response of the reinforced membrane.

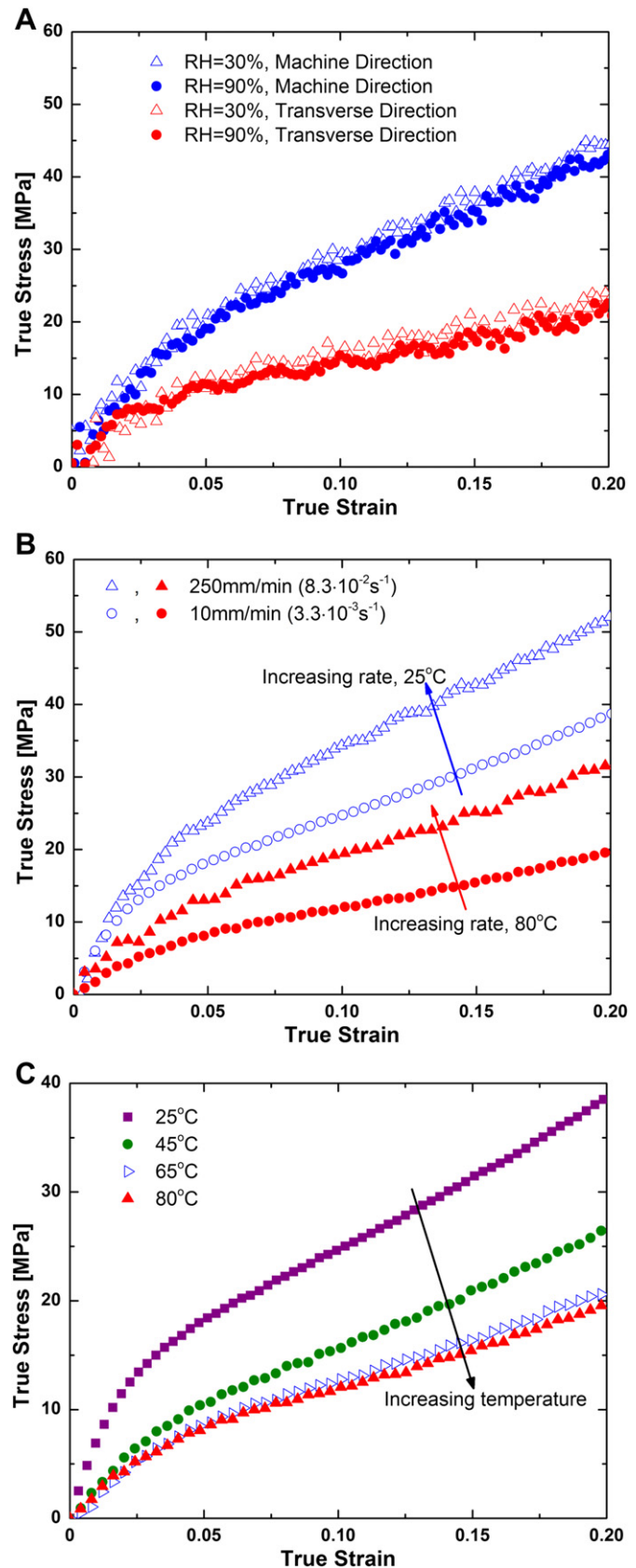


Fig. 2. Selected experimental data showing true-stress vs. true-strain results for uniaxial tensile test measurements for various (A) hydration levels, (B) load rates, and (C) temperatures.



The constitutive material parameters are all functions of temperature and strain rate (wherever applicable) as determined from the experiments.

We assume that the total strain tensor,  $\varepsilon_{ij}$ , is given as the sum

$$\varepsilon_{ij} = \varepsilon_{ij}^S + \varepsilon_{ij}^T + \varepsilon_{ij}^M; \quad (i, j = 1, 2, 3), \quad (1)$$

where  $\varepsilon_{ij}^S$ ,  $\varepsilon_{ij}^T$  and  $\varepsilon_{ij}^M$  are the swelling, thermal and mechanical strain contributions, respectively. The swelling and the thermal strain formulations have been discussed in our previous work [32], but are summarized in Appendix A.1 and A.2 for completeness. The mechanical strains ( $\varepsilon_{ij}^M$ ) are defined in the context of a three-network viscoelastic-plastic model, Fig. 5, where one network corresponds to the time-independent, elastic–plastic response and the other two networks correspond to the time-dependent, elastic-viscous response. By definition, the total mechanical strain,  $\varepsilon_{ij}^M$ , is equal in all three networks

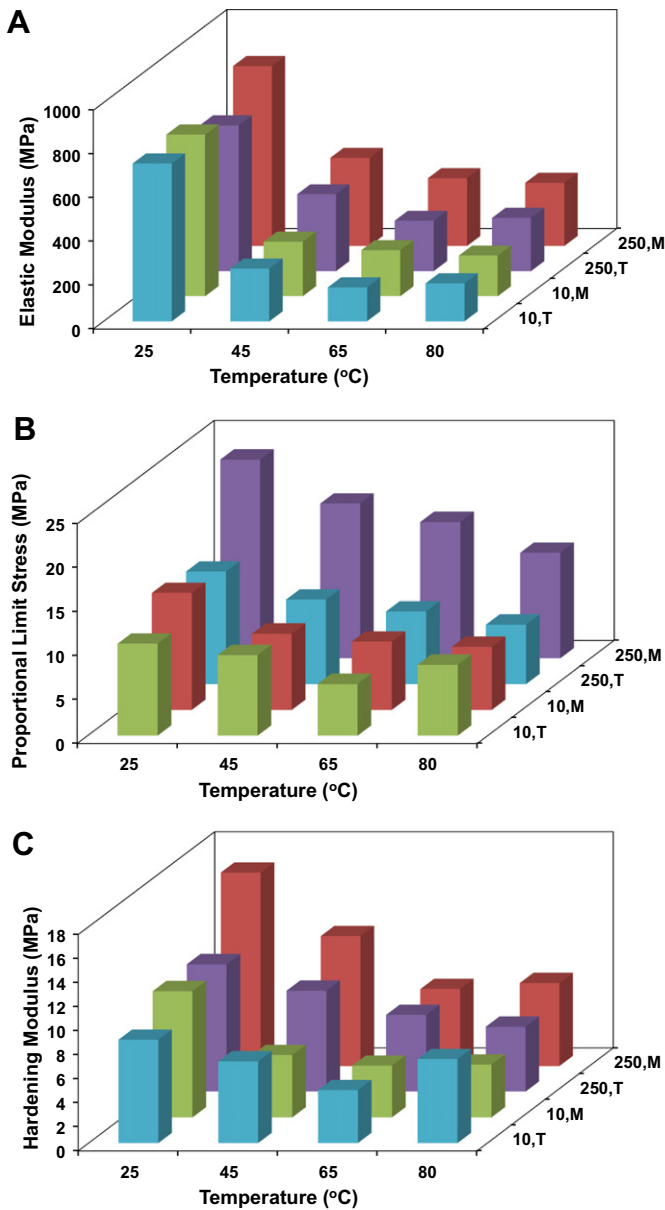


**Fig. 3.** (A) elastic modulus, (B) proportional limit stress, and (C) hardening modulus for the reinforced membrane at various temperatures for two load rates (10 and 250 mm min<sup>-1</sup>) and two directions of loading (M-Machine and T-Transverse).

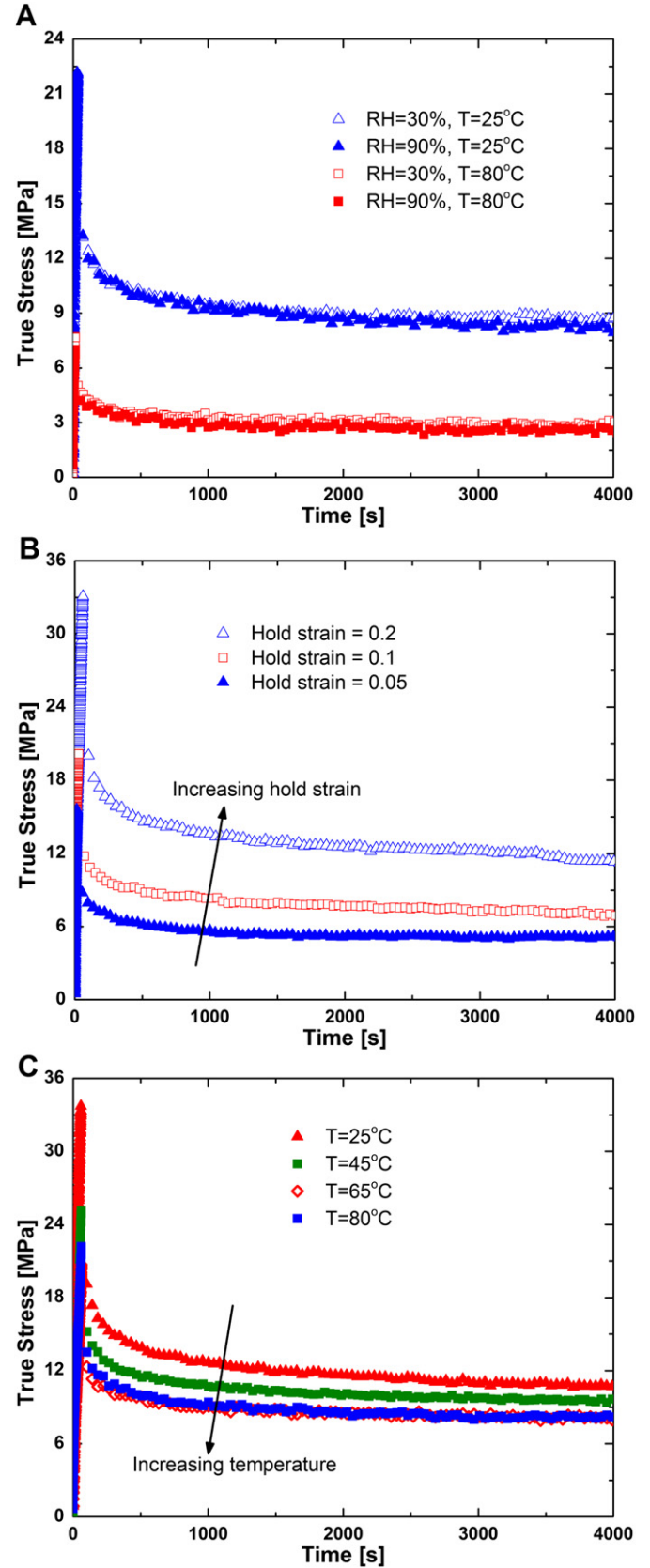


**Fig. 4.** Sample experimental data showing true-stress vs. time evolution for various (A) hydration levels (at two hold strains of 0.05 and 0.1), (B) holding strains (at a temperature of 25 °C), and (C) temperatures (at a hold strain of 0.2).

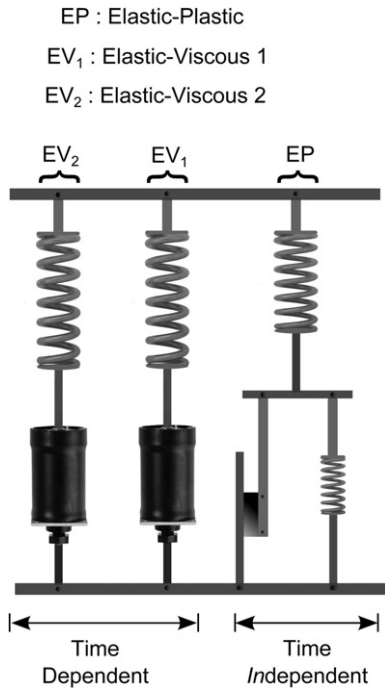


Fig. 5. One-dimensional idealization of the three-network viscoelastic-plastic constitutive model.

$$\epsilon_{ij}^M = \epsilon_{ij}^{EP} = \epsilon_{ij}^{EV_1} = \epsilon_{ij}^{EV_2}, \quad (2)$$

where the superscripts EP, EV<sub>1</sub> and EV<sub>2</sub> refer to the elastic–plastic, the first elastic–viscous network and the second elastic–viscous network of the model, respectively (Fig. 5). The strain formulations for the elastic–plastic (EP) network and the first elastic–viscous (EV<sub>1</sub>) network are discussed in our previous work [32] and summarized in Appendix A.3 and A.4, respectively, while the following discussion describes the strains in the elements of the second elastic–viscous (EV<sub>2</sub>) network.

The total strain in the second elastic–viscous (EV<sub>2</sub>) network is the sum of the strain in the spring and the dashpot element given by

$$\epsilon_{ij}^{EV_2} = (\epsilon_{ij}^{EV_2})_{el} + (\epsilon_{ij}^{EV_2})_{vi}, \quad (3)$$

Table 1

(A) elastic–plastic and (B) elastic–viscous, constitutive model parameters for the e-PTFE reinforced PFSA membrane material.

A						
Temp (°C)	$K_{EP}$ (MPa)	$\sigma_y$ (MPa)	H (MPa)	$K_{EV_1}$ (MPa)		$K_{EV_2}$ (MPa)
				10 mm min <sup>-1</sup>	250 mm min <sup>-1</sup>	
25	200	5	150	539	622	8.3
45	120	4	100	130	274	4.8
65	100	4	72	111	211	3.9
80	86	3	60	100	204	3.2
B						
Temp (°C)	ln(A)		n	B		m
	10 mm min <sup>-1</sup>	250 mm min <sup>-1</sup>		10 mm min <sup>-1</sup>	250 mm min <sup>-1</sup>	
25	−23.03	−23.03	8	7	50	6.4
45	−20.72	−23.03	8	7	50	5.5
65	−17.32	−19.11	8	6.8	50	3.3
80	−18.42	−20.72	8	6.5	50	2.6

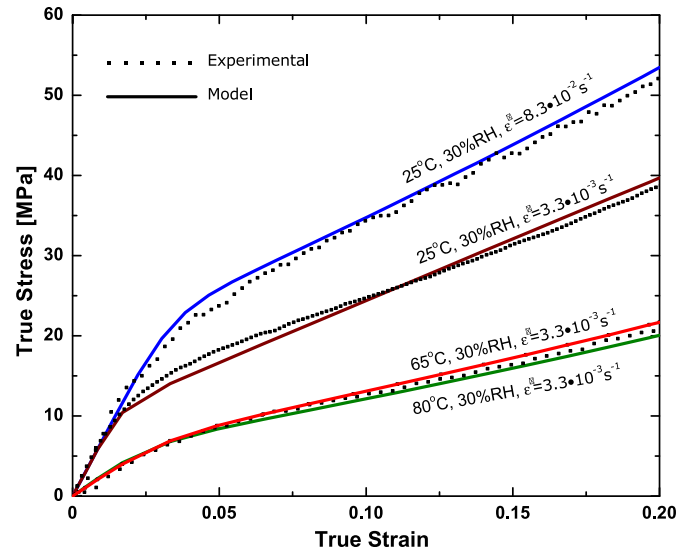


Fig. 6. True-stress vs. true-strain uniaxial tensile response of the reinforced membrane material at various conditions obtained from constitutive model predictions compared with the experiments.

where subscript el refers to the elastic portion and vi refers to the viscous portion of the strain. Assuming a Neo–Hookean hyperelastic formulation for the constitutive response of the spring in this network [37], the Cauchy stress,  $\sigma_{ij}^{EV_2}$ , is given by

$$\sigma_{ij}^{EV_2} = \frac{\mu}{J} \text{dev}[b_{ij}] + \kappa(J-1)\delta_{ij}, \quad (4)$$

where  $\mu = K_{EV_2}/2(1+\nu)$  and  $\kappa = K_{EV_2}/3(1-2\nu)$  are the shear and bulk modulus respectively, with  $K_{EV_2}$  being the elastic modulus. The tensor  $b_{ij}$  is the distortional left-Cauchy Green tensor given by  $J^{-2/3}F_{ik}F_{jk}$  and the Jacobian,  $J$ , is given by  $\det(F)$ , where  $F$  is the deformation gradient.

The dashpot in this network follows Hill's criteria [38] to model anisotropic viscous behavior. The generalized three-

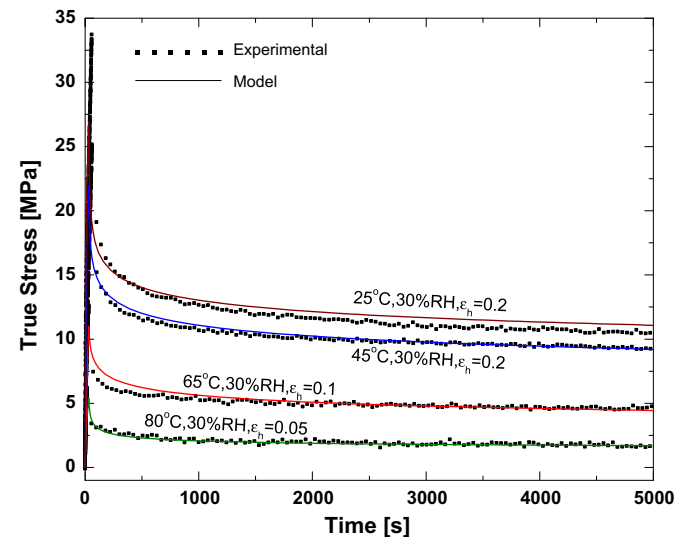


Fig. 7. True-stress evolution as a function of time for the uniaxial stress–relaxation test of the reinforced membrane material at various conditions obtained from constitutive model predictions compared with the experiments.

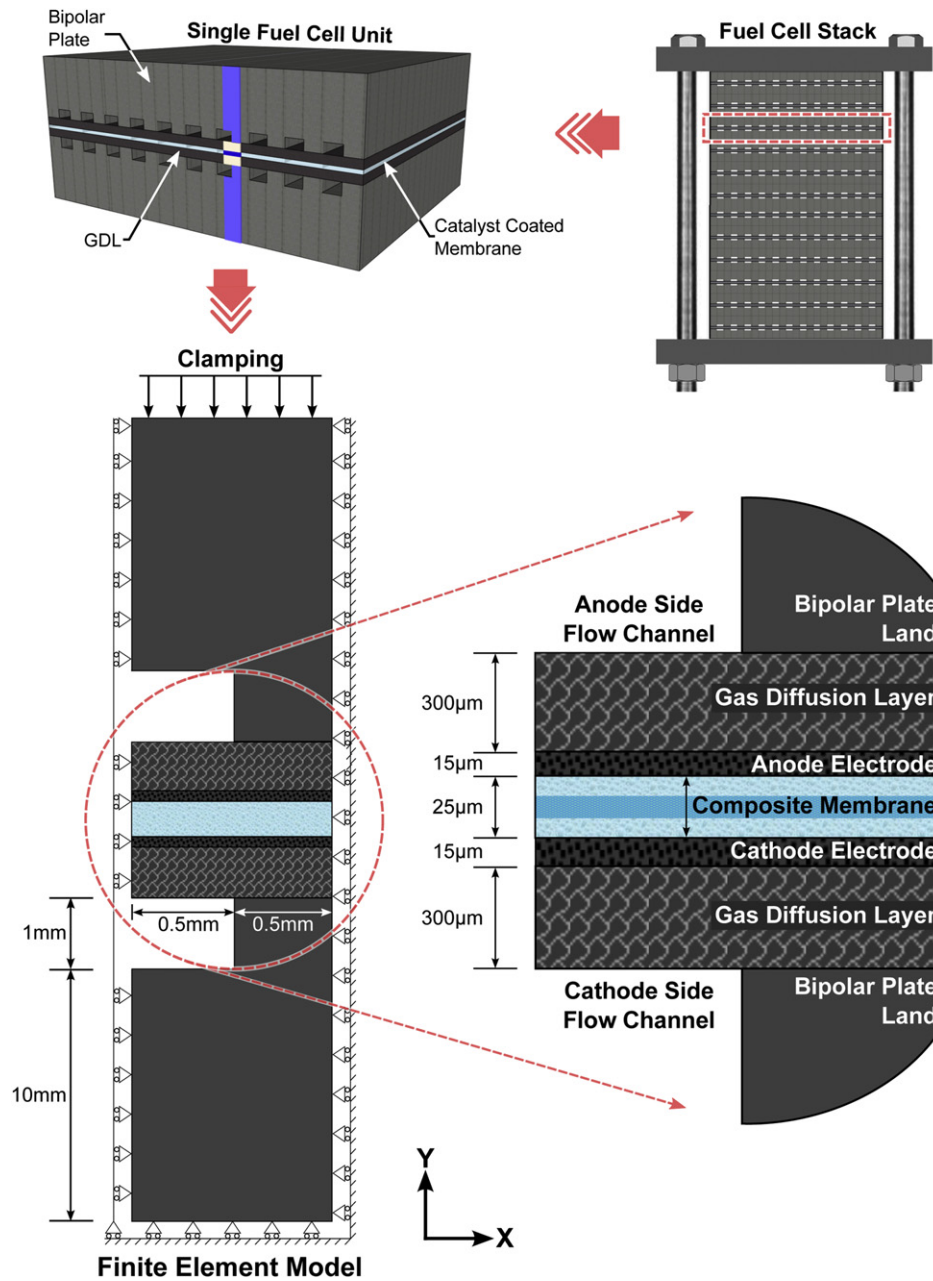


Fig. 8. Schematic of the 2D generalization of a single fuel cell unit used to conduct composite membrane simulations (not to scale).

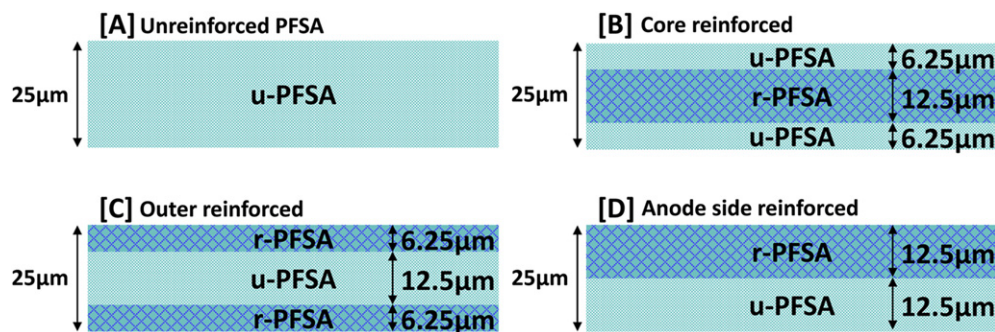


Fig. 9. Schematic configurations of the composite membrane with various arrangements of the reinforcement layer. (A) unreinforced PFSA (reference), (B) core-reinforced, (C) outer-reinforced, and (D) anode side reinforced configuration. u-PFSA and r-PFSA refer to unreinforced and reinforced membrane material, respectively.

**Table 2**

Material properties for various fuel cell components used in the finite element model.

	Behavior	Properties	Swelling behavior	Thermal expansion
Reinforced membrane	Viscoelastic-plastic	Section 2.3	Transverse isotropic ( $\epsilon_{\text{out-of-plane}}^{\text{sw}} = 10\epsilon_{\text{in-plane}}^{\text{sw}}$ )	$1.2 \cdot 10^{-8} \text{ K}^{-1}$
Unreinforced membrane	Viscoelastic-plastic	[32]	Isotropic ( $\epsilon_{\text{out-of-plane}}^{\text{sw}} = \epsilon_{\text{in-plane}}^{\text{sw}}$ )	$1.2 \cdot 10^{-8} \text{ K}^{-1}$
Catalyst	Viscoelastic-plastic	[47]	Assumed not to swell	Neglected
GDL	Transverse isotropic, linear-elastic	$E_{11} = 1500 \text{ MPa}$ $E_{22} = 9 \text{ MPa}$ [48]	Assumed not to swell	Neglected
Bipolar plate	Linear-elastic	$E = 10 \text{ GPa}$ , $\nu = 0.25$ [25]	Assumed not to swell	Neglected

dimensional form of the flow rate for the dashpot in this network is given by

$$\left(\dot{\epsilon}_{ij}^{\text{vi}}\right) = \left(\frac{\sigma^{\text{Hill}}}{B}\right)^m, \quad (5)$$

where  $m$  is the flow exponent and  $B$  is the flow resistance in this network. The Hill stress,  $\sigma^{\text{Hill}}$  is given by

$$\sigma^{\text{Hill}} = \sqrt{F(\sigma_{22} - \sigma_{33})^2 + G(\sigma_{33} - \sigma_{11})^2 + H(\sigma_{11} - \sigma_{22})^2 + 2L\sigma_{23}^2 + 2M\sigma_{31}^2 + 2N\sigma_{12}^2} \quad (6)$$

where  $F$ ,  $G$ ,  $H$ ,  $L$ ,  $M$  and  $N$  are the Hill parameters determined by experiment.

The parameters of the three-network viscoelastic–plastic constitutive model discussed above were obtained from the experimental data for the reinforced membrane material, and are given in Table 1. To verify that these material parameters correspond to the mechanical properties of the membrane, finite element simulations of a membrane-strip model using the above discussed constitutive behavior were compared with the experimentally obtained stress–strain and relaxation results (Figs. 6 and 7). A plane stress ABAQUS [39] FE model was developed with dimensions conforming to the test specimen. The simulation matches the experimental results fairly well and captures key features of the tensile response such as elastic modulus, onset of non-linearity, and hardening modulus (Figs. 6 and 7). In the stress–relaxation results, the simulation captures the stress peak, relaxation time and the equilibrium stress for the observed time frame of about 1–1.5 h. The trend suggests that relaxation continues beyond the test time, although at a decreasing rate. (Due to limitations of the testing equipment and practical considerations, relaxation beyond 1.5 h was not measured.)

### 3. Numerical implementation

In this section, the mechanical response of a composite PFSA membrane in a fuel cell subjected to hygrothermal cycling is investigated via finite element simulations. We used the commercial software ABAQUS<sup>TM</sup> [39] with 8-noded biquadratic coupled temperature-displacement generalized plane strain elements (CPEG8T). The model consists of 32,604 elements and 101,424 nodes with 20 elements along the thickness direction of the composite membrane. Numerical convergence was verified using progressively finer meshes until no appreciable change was observed in the results.

#### 3.1. Geometry

A typical fuel cell unit contains repetitive grooves and lands forming the gas channels in the bipolar plate. Therefore, we

constructed a model for a representative repeating element adapted from our previous work [25,32,35,40] consisting of a half of a land and a half of a groove with the dimensions given in Fig. 8. Generalized plane strain conditions are assumed, corresponding to a uniform strain in the  $z$ -direction (out-of-plane in the figure). The right edge and bottom have symmetric boundary conditions imposed. To account for possible displacement in the in-plane ( $x$ )

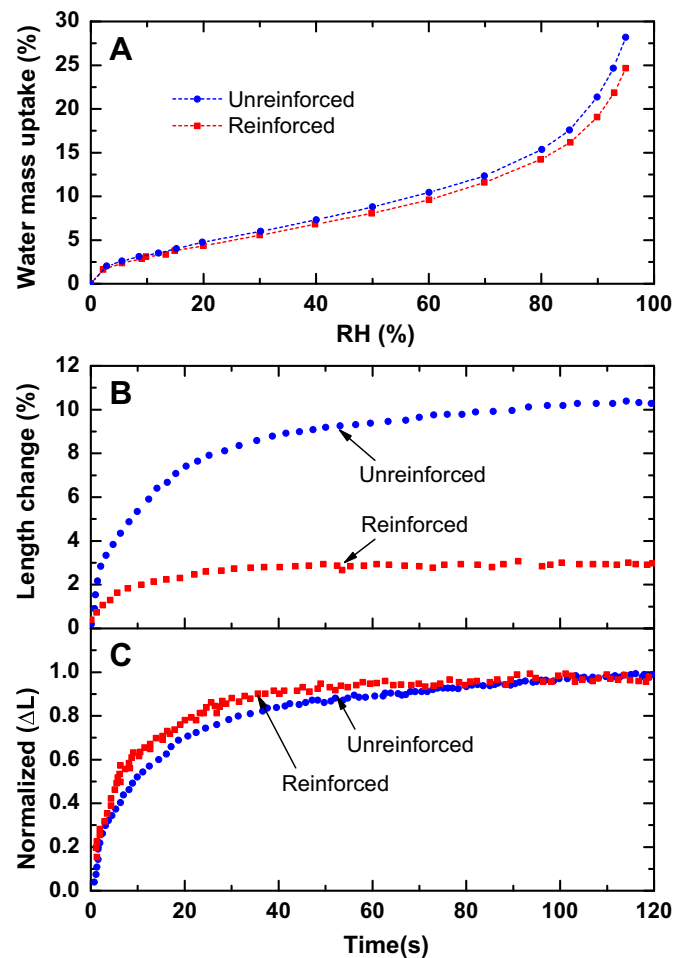


**Fig. 10.** (A) equilibrium water mass uptake for the unreinforced and the reinforced membrane material at 80 °C. (B) in-plane length change (%) and (C) length change after normalizing by the final equilibrium length, for both the materials. The data is based on Griffith et al. [41].



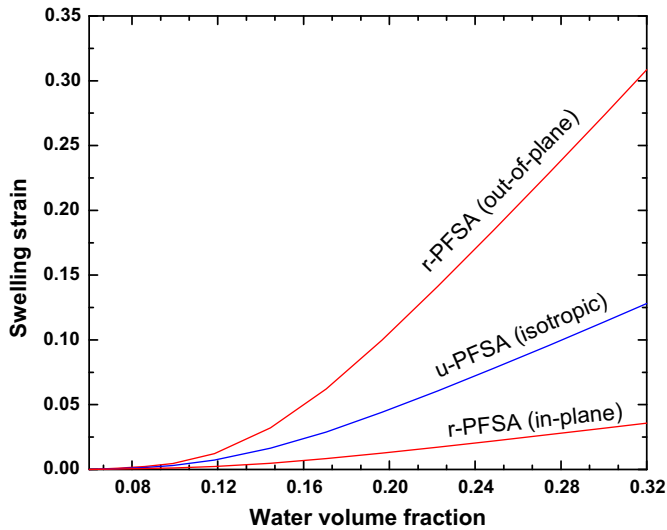


**Fig. 11.** Transversely isotropic swelling strain in the reinforced (r-PFSA) membrane material and isotropic swelling strain in the unreinforced (u-PFSA) membrane material as functions of water volume fraction.

direction, a continuous boundary condition is applied, under which all the nodes on left edge of the model can move laterally in unison. A uniform pressure of 1 MPa is applied on the top edge of the bipolar plate to simulate a typical spring-loaded clamping pressure

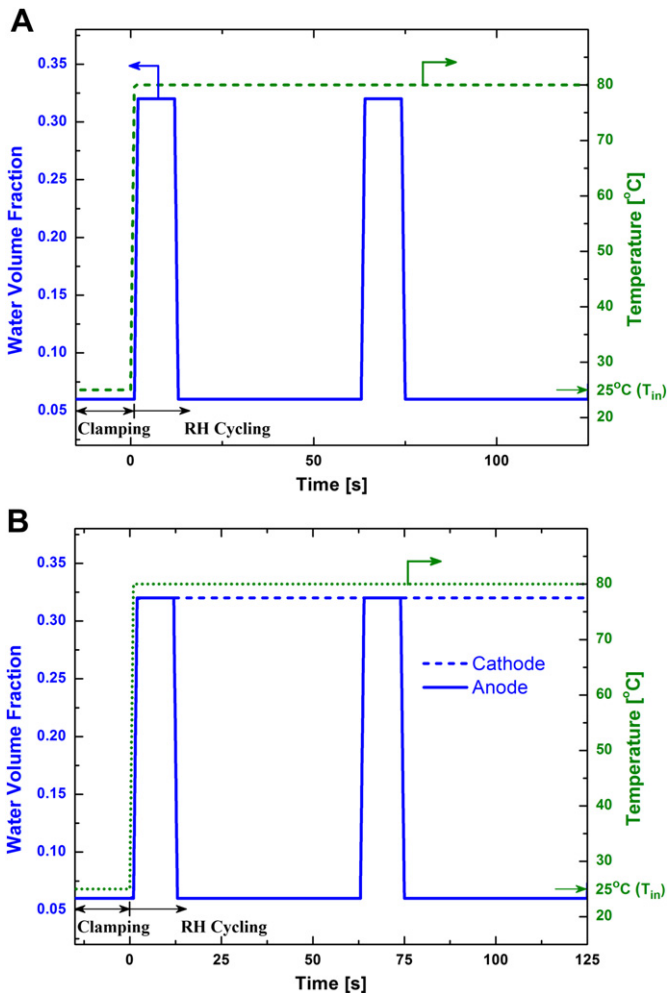


**Fig. 12.** (A) symmetric RH cycling test profile and (B) asymmetric RH cycling profile.

		Max. Stress [MPa]	
		u-PFSA	r-PFSA
In plane	tensile	8.22	0.3
	compressive	-9.75	-10.97
Out-of plane	tensile	0	0
	compressive	-0.2	-0.2

**Fig. 13.** Maximum tensile and maximum compressive stresses (MPa) in the in-plane and the out-of-plane directions for the unreinforced and the reinforced membrane materials.

for a fuel cell. The effect of altering the clamping pressure is also investigated parametrically in Section 4.

The composite membrane is modeled as a layered structure consisting of two materials (unreinforced PFSA and reinforced PFSA) arranged in four configurations (Fig. 9):

- Unreinforced membrane (u-PFSA) material only (reference case) (Fig. 9A).
- Reinforced (r-PFSA) membrane material as the core surrounded by two layers of unreinforced membrane material on the outside (Fig. 9B).
- Unreinforced membrane material as the core surrounded by two layers of reinforced membrane material on the outside (Fig. 9C).
- Reinforced membrane material on the anode side and unreinforced membrane material on the cathode side (Fig. 9D).

During manufacturing, the various layers are produced together using a casting process. Therefore, the layers are connected in the fuel cell model using a 'tie constraint' [39] in which the interface nodes are constrained to move together (i.e. no interfacial debonding).

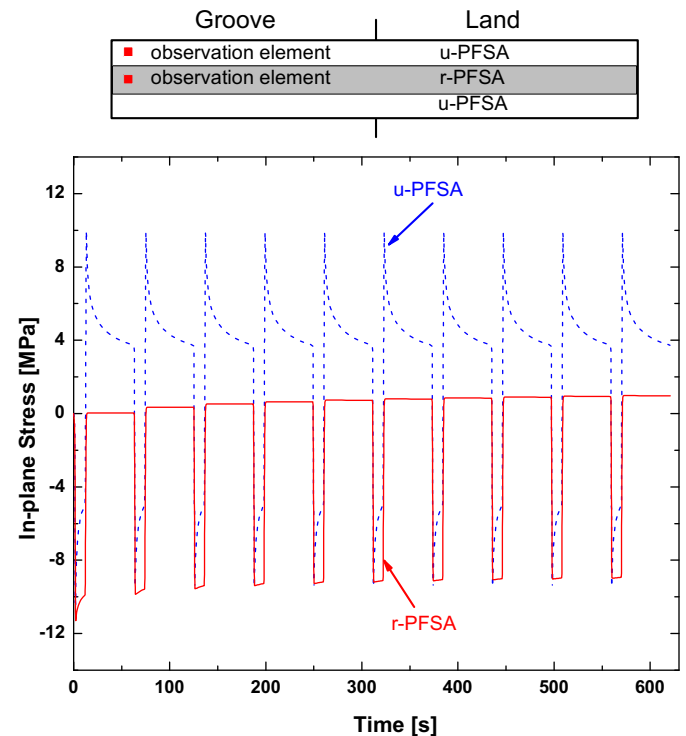


**Fig. 14.** Symmetric RH cycle: In-plane stress evolution for an element each on the groove side in the unreinforced and the reinforced layers of the core-reinforced composite membrane configuration for ten cycles. u-PFSA and r-PFSA refer to the unreinforced and the reinforced membrane materials, respectively.



### 3.2. Properties

The material properties used for the various fuel cell components in the finite element model are summarized in Table 2. The membrane is the only component that is assumed to swell. The sorption and swelling behavior used in the model of the membrane is described in the following section.

#### 3.2.1. Sorption behavior

The water sorption and the consequent swelling behavior of the membrane used in this work is based on the equilibrium water mass uptake and in-plane swelling data measured by Griffith et al. [41]. In this experiment, the membranes were exposed to an outside humidity change from dry ( $\lambda = 2$ ) to saturated ( $\lambda = 14$ ) condition (at a constant temperature of 80 °C), while the increase in mass and change in length were measured. The data (Fig. 10A) show that the e-PFTE reinforcement does not significantly affect the total water mass uptake [41]. However, dimensional changes in the in-plane direction are significantly different as shown by the in-plane swelling measurements [41] (Fig. 10B). The reinforced membrane swells considerably less in the in-plane direction than the unreinforced membrane. (The out-of-plane swelling can be approximated by considering the total water uptake of the reinforced membrane; Fig. 10A.) After normalizing by the equilibrium length, the swelling kinetics of the two membranes appears to be

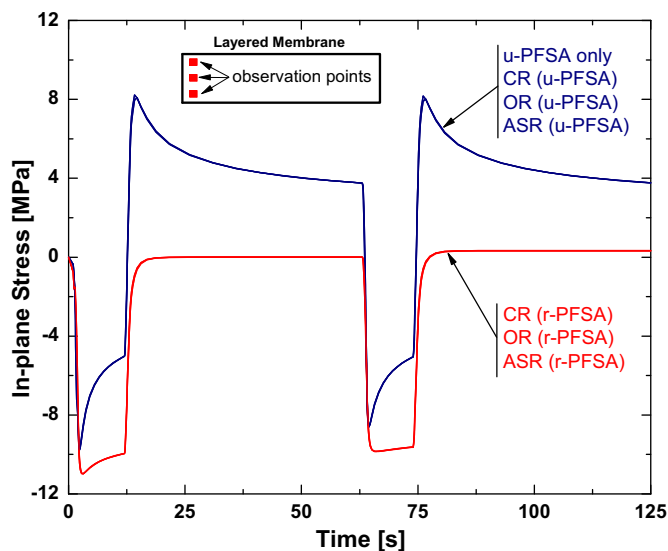
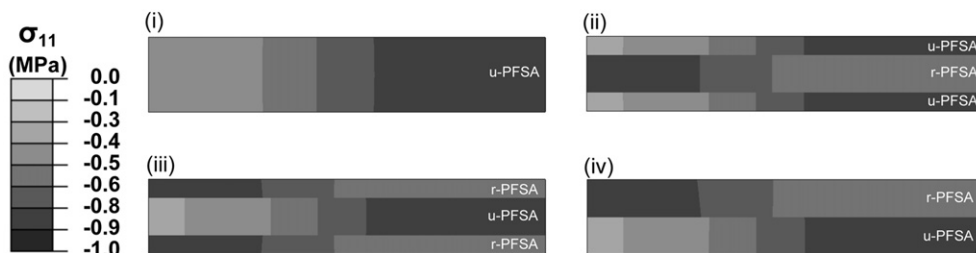
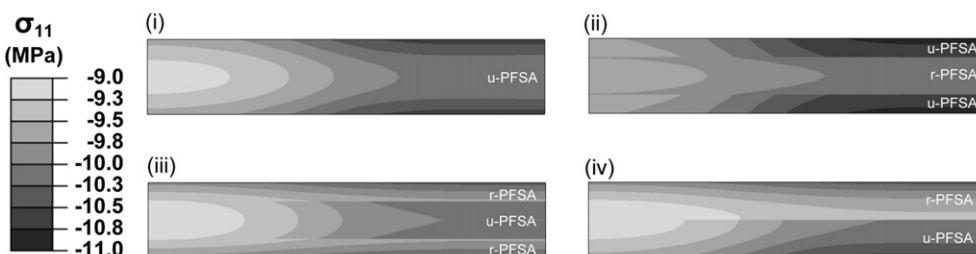


Fig. 16. Symmetric RH cycle: In-plane stress evolution over two cycles in the groove side elements for the unreinforced (u-PFSA) and reinforced (r-PFSA) layer of the composite membrane. CR, OR and ASR refer to core-reinforced, outer-reinforced and anode side reinforced configurations, respectively.

#### A. Maximum in-plane stress after clamping



#### B. Maximum in-plane stress after hydration



#### C. Maximum in-plane stress after dehydration

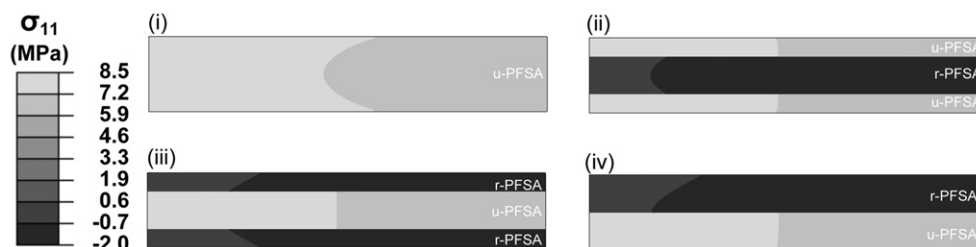
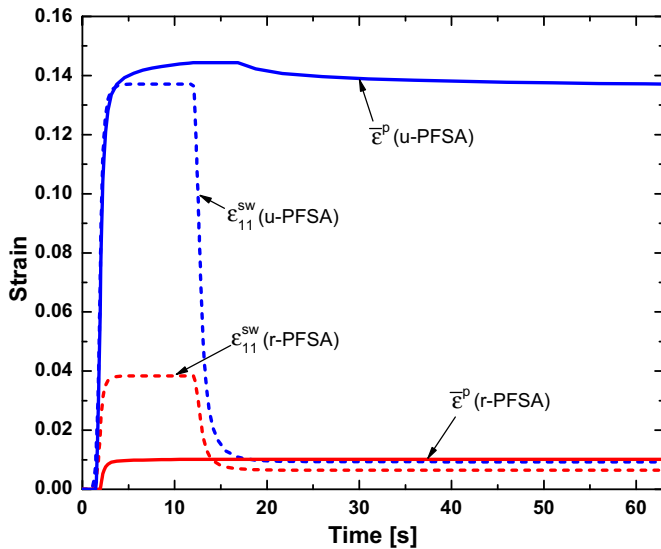


Fig. 15. Symmetric RH cycle: Snapshots of maximum in-plane stress contours in the composite membrane after (A) clamping, (B) hydration, and (C) dehydration step. (i)–(iv) refer to the four, layered configurations as shown in Fig. 10 u-PFSA and r-PFSA refer to the unreinforced and the reinforced membrane materials, respectively.



**Fig. 17.** Symmetric RH cycle: In-plane swelling strain,  $\epsilon_{11}^{sw}$ , and the total plastic strain magnitude,  $\bar{\epsilon}^p$ , evolution for an element from the groove side each in the unreinforced (u-PFSA) and the reinforced (r-PFSA) layer of the composite membrane.

similar in nature as shown in Fig. 10C. Therefore, in the numerical analyses that follow, sorption kinetics of the reinforced membrane and unreinforced membrane are assumed to be similar.

The experiments show that the in-plane swelling in the reinforced membrane is about a quarter of that of the unreinforced membrane [41]. If we assume that the swelling of the unreinforced membrane is isotropic, then the out-of-plane swelling of the reinforced membrane is approximately ten times larger than its in-plane swelling as shown in Fig. 11, to account for the nearly equal total water uptake. Therefore, we assumed transversely isotropic swelling behavior, with out-of-plane swelling equal to ten times than that of in-plane swelling, for the reinforced material in the finite element simulations.

### 3.3. Load cases

A relative humidity (RH) cycling test has been developed by W. L. Gore [28] as an accelerated test protocol to assess the mechanical durability of fuel cell membranes. This cycle operates at a constant temperature of 80 °C, while the humidity is cycled between dry (RH ~ 15%) and supersaturated (corresponding to wet gas dewpoint of 90 °C) vapor conditions. The hygrothermal cycling load cases investigated in this work are based on this cycle, referred to as the “Gore cycle”. In particular, two load cases are considered in this work:

#### 3.3.1. Symmetric RH cycle

The standard Gore cycle, with simultaneous application of equally humidified nitrogen on both the anode and the cathode side gas channels is referred to as ‘Symmetric RH Cycle’ in this work

**Table 3**

Symmetric RH cycling: Maximum in-plane residual tensile stress (in MPa) in the unreinforced (u-PFSA) and the reinforced (r-PFSA) membrane material for various thicknesses of u-PFSA with a constant reinforcement core thickness (5  $\mu$ m).

	Thickness of the unreinforced segment			
	1 $\mu$ m	5 $\mu$ m	10 $\mu$ m	20 $\mu$ m
u-PFSA	10.38	10.27	10.13	9.85
r-PFSA	0.04	0.04	0.03	0.01

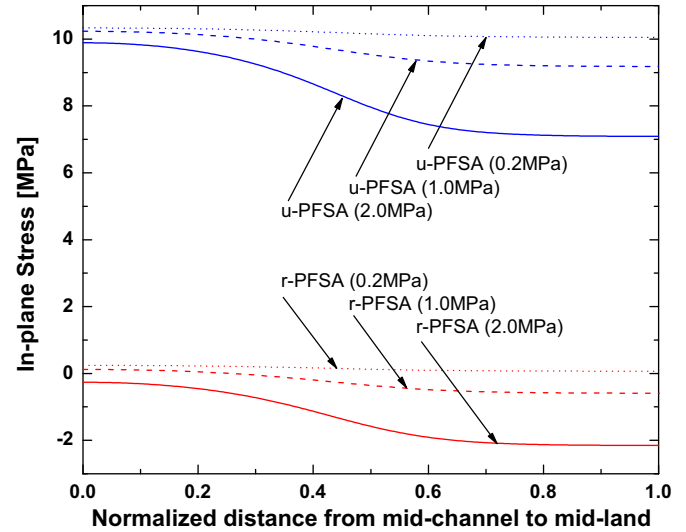


**Fig. 18.** Symmetric RH cycle: Distribution of the in-plane stress after dehydration as a function of the normalized distance from mid-channel to mid-land for three values of clamping pressure: 0.2, 1.0 and 2.0 MPa. u-PFSA and r-PFSA correspond to the unreinforced and the reinforced layers of the composite membrane.

(Fig. 12A). The maximum water volume fraction,  $\phi$ , corresponding to saturated vapor conditions is 0.32. Using equation (A-2), this corresponds to water content in the membrane ( $\lambda$ ) of approximately 14. The water volume fraction for the dry state corresponds to  $\phi = 0.06$  (or  $\lambda = 2$ ). The loading is applied at the GDL interface in the channels for 10 s corresponding to the wet state and 50 s for the dry state. The transition from dry to wet and vice-versa is assumed to be linear and takes place in a very short time (1 s in the simulation).

#### 3.3.2. Asymmetric RH cycle

In a working fuel cell drawing current, equal saturation at the anode and the cathode is unlikely. The generation of water tends to keep the cathode side hydrated and the electro-osmotic drag tends to dry-out the anode side with increasing current density [42]. Therefore, an ‘Asymmetric RH Cycle’ was investigated which involves different RH loading at the anode and the cathode sides flow channels thus producing a water content gradient across the membrane thickness (Fig. 12B). In this cycle, the cathode side flow channel is kept hydrated at all times while humidity cycling following the Gore cycle (described above) is applied at the anode side flow channel (Fig. 12B).

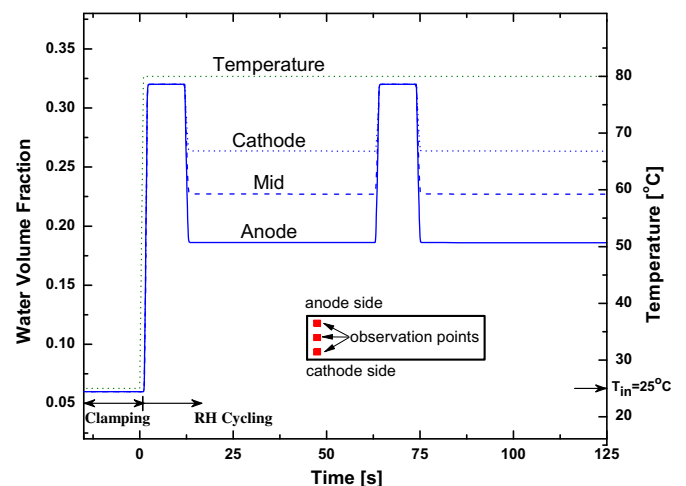


**Fig. 19.** Water and temperature profile in the membrane for asymmetric RH loading.

In both the load cycles, humid and dry nitrogen is alternately introduced into the flow channels. The actual water profile at the membrane is mediated by the diffusion through GDL, electrode and the composite membrane itself. The water volume fraction in the membrane is modeled as a third degree of freedom in addition to the two nodal displacements in the two-dimensional generalized plane strain element used for the finite element analysis. Therefore, a coupled sorption-displacement analysis is carried out in which the swelling-induced stresses and the water uptake through diffusion are coupled and solved simultaneously [43].

#### 4. Results and discussion

The hydration load on the membrane leads to volumetric swelling from the water absorption. However, the swelling is limited due to the mechanical constraints from the other fuel cell components and consequently, gives rise to stresses. In our previous work [25,32,43,44] we showed that the in-plane stresses are the dominant components in the unreinforced membrane during fuel cell operation. This holds for the composite membrane

as illustrated by the relative stress magnitudes in the membrane for a typical simulation (Fig. 13). Consequently, only the in-plane stress component will be discussed in the following.

##### 4.1. Symmetric loading

The typical in-plane stress evolution in the unreinforced and the reinforced layers of the core-reinforced composite membrane configuration, for ten cycles of symmetric RH cycling is shown in Fig. 14. The evolution is presented for a representative element in each of the two layers of the composite membrane on the groove side. While both layers develop similar compressive stresses after hydration, the residual tensile stress in the reinforced membrane material is significantly lower compared to the unreinforced material. This can be attributed to the greater hydration-dependence of the material properties for the unreinforced membrane. The peak stresses increase for the initial few cycles and become constant thereafter.

A more detailed understanding of the stress evolution may be obtained by studying the snapshots of the in-plane stress contours

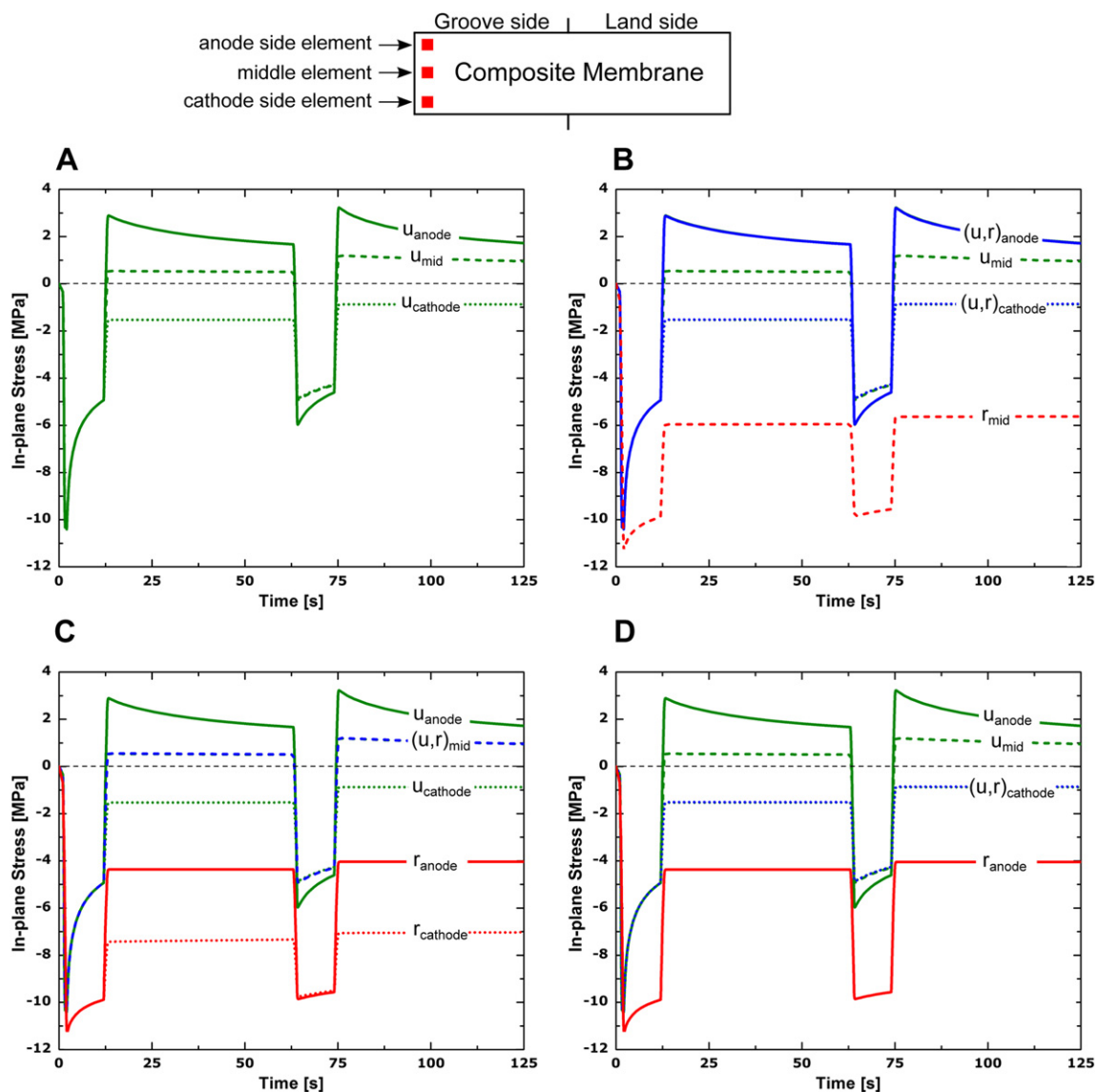
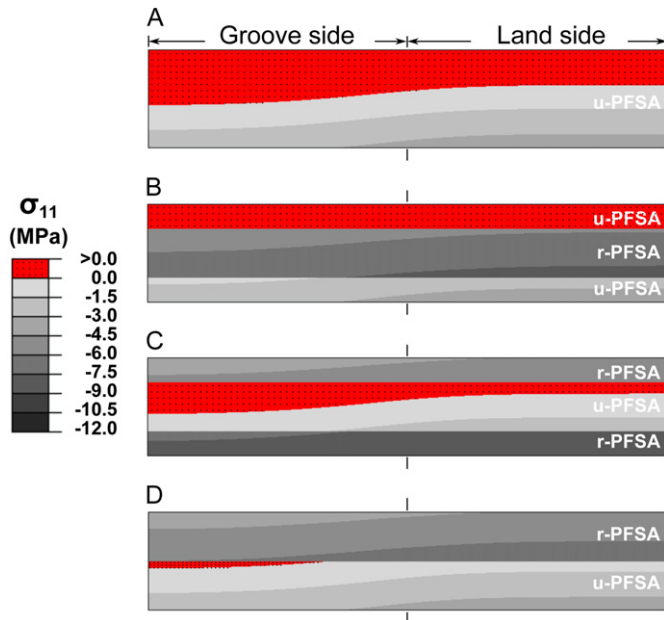


Fig. 20. Asymmetric RH cycling: In-plane stress evolution for three elements (shown at the top) on the groove side of the composite membrane for (A) unreinforced PFSA only (reference case), (B) core-reinforced, (C) outer-reinforced, and (D) anode side reinforced configurations.



**Fig. 21.** Asymmetric RH cycling: Snapshots of the in-plane stress contours in the composite membrane after dehydration, highlighting the residual tensile stresses developed in various configurations (A–D) as shown in Fig. 10. u-PFSA and r-PFSA correspond to the unreinforced and the reinforced layers of the composite membrane.

in the composite membrane for symmetric RH cycling (Fig. 15). The stress evolution over time for three elements on the groove side of the composite membrane is also shown (Fig. 16). After the clamping pressure (1 MPa) is applied, small compressive stresses appear throughout the composite membrane (Fig. 15A). When the temperature is increased from the initial 25 °C to 80 °C along with the increase in hydration from the initial dry state ( $\phi = 0.06$ ) to saturated vapor ( $\phi = 0.32$ ), high compressive stresses develop in both layers of the composite membrane, with the magnitude being higher in the reinforced layer (Fig. 15B). The region under the land has higher compressive stress than the region under the groove. The system is then held for 10 s at the maximum hydration during which relaxation of the in-plane stress occurs (Fig. 16). When the system is dehydrated back to the dry state, the membrane shrinks. The unreinforced layer develops large tensile stresses after dehydration while very small residual tensile stresses develop in the reinforced layer of the composite membrane (Fig. 15C).

Due to the low in-plane swelling and relatively larger proportional limit stress, the reinforced membrane develops lower in-plane swelling strain and lower total plastic strain than the unreinforced layer (Fig. 17). Therefore, the reinforcement layer will most likely reduce (or delay) the formation of pinholes and through-cracks.

#### 4.1.1. Effect of thickness

Simulations for configurations having different unreinforced outer layer thickness (1, 5, 10 and 20  $\mu\text{m}$ ) with a constant reinforced core thickness (5  $\mu\text{m}$ ) were investigated. The results for symmetric

RH cycling show that the resulting maximum residual tensile stress after dehydration decreases marginally with increased thickness of the outer layer, Table 3.

#### 4.1.2. Effect of clamping pressure

The effect of clamping pressure on the membrane stresses is investigated for three different clamping loads (0.1, 1.0 and 2.0 MPa) applied on top of the bipolar plate. The larger clamping pressure induces larger compressive stresses during hydration in the membrane and consequently, lower residual tensile stress after dehydration (Fig. 18). This suggests that, higher clamping pressure may have a beneficial effect on membrane life.

#### 4.2. Asymmetric loading

Fig. 16 shows that the stress evolution in the composite membrane is independent of the relative location of the reinforcement layer. This is due to the fact that the stresses result from the swelling strains, which are driven by equal RH loading from both sides of the membrane. The stresses in the various layers would depend on the layering geometry in the presence of: (i) any geometric perturbations (such as cracks or debonding) or (ii) asymmetric RH loading from the opposite sides of the membrane. While the case of geometric perturbations is left for a future study, we investigate asymmetric RH loading (Section 3.3) in the following.

The resulting water and temperature profiles in the membrane are as shown in Fig. 19 for an asymmetric RH cycle applied at the gas channels. The stress results in Fig. 20 are provided for three elements, each located at 4  $\mu\text{m}$  from the left boundary. The y-location of the elements is 3  $\mu\text{m}$  from the membrane–anode interface, mid-plane, and 3  $\mu\text{m}$  from the membrane–cathode interface. The results suggest that the stresses on the anode side of the membrane are higher than on the cathode side due to the larger variation in hydration on the anode side.

In all the layering configurations, the reinforced material develops large compressive stresses throughout after hydration. However, no residual tensile stresses develop in the reinforced material after dehydration (Fig. 20B–D). On the other hand, in the unreinforced layer of the core-reinforced configuration (Fig. 20B), the maximum residual tensile stress is similar to the stress magnitude in the reference configuration (Fig. 20A). This can be explained by the fact that the unreinforced material is on the outside of the composite membrane and is therefore exposed to similar humidity cycling as in the reference case.

For the outer-reinforced configuration (Fig. 20C), the maximum stress in the unreinforced layer is equal to the maximum stress reached in the middle of the membrane in the reference case. In the anode-reinforced configuration, in which the reinforcement is on the anode side (Fig. 20D), the in-plane residual stress in the unreinforced layer is similar to the stress level on the cathode side of the membrane in the reference case. The anode side reinforced configuration develops the lowest magnitude of residual in-plane tensile stresses, which are concentrated on a smaller region in the unreinforced layer of the composite membrane (Fig. 21).

A summary of the maximum residual tensile stresses in the unreinforced and the reinforced layers of the composite membrane

Configuration	Symmetric RH cycling		Asymmetric RH cycling	
	u-PFSA	r-PFSA	u-PFSA	r-PFSA
Unreinforced only	8.1	-	3.8	-
Core-reinforced	8.2	0.3	3.8	-5.1
Outer-reinforced	8.1	0.3	1.9	-3.8
Anode side reinforced	8.2	0.3	0.4	-3.8

**Fig. 22.** Maximum residual in-plane stress (in MPa) in the unreinforced (u-PFSA) and the reinforced (r-PFSA) layers of the membrane for the investigated configurations.



for the various configurations is provided in Fig. 22. The residual tensile stresses in the unreinforced material, in the case of asymmetric cycling, depend on the relative arrangement of the two membrane material layers, with the anode-side reinforced configuration leading to lowest maximum tensile stress level (10% of the reference case maximum stress).

## 5. Concluding remarks

In this work, the time-dependent mechanical properties of an e-PTFE reinforced experimental membrane material have been investigated for a range of environmental and loading conditions using uniaxial tensile and stress–relaxation tests. The constitutive response of the reinforced material is characterized using a three-network viscoelastic-plastic model.

To investigate how the reinforcement would affect the mechanical stresses in an operating fuel cell membrane, a composite membrane consisting of the unreinforced PFSA and the e-PTFE reinforced PFSA material in layered geometries was simulated. The constitutive model for the reinforced membrane material was incorporated into a finite element model representing a single fuel cell unit assembly. The fuel cell FE analysis was conducted as a coupled sorption-displacement problem [32,43] enabling us to model the water content profile and mechanical stresses simultaneously. The stress evolution for various configurations of the composite membrane as well as the effects of symmetric RH cycling, asymmetric RH cycling, membrane thickness and clamping pressure were investigated.

The results of the simulations show that (i) the reinforced material in the composite membrane develops large compressive stresses after hydration but significantly lower residual in-plane stresses after dehydration when compared to the unreinforced membrane material; (ii) the relative arrangement of the reinforcement in the composite membrane does not affect the maximum in-plane stress in the unreinforced layer during symmetric RH cycling; (iii) the total plastic strain magnitude in the reinforced layer is significantly lower than in the unreinforced layer; (iv) increasing the thickness of the unreinforced layer decreases the residual in-plane tensile stresses in both the layers of the composite membrane; (v) an increase in the clamping pressure leads to lower maximum residual in-plane tensile stresses; (vi) during asymmetric RH cycling, the anode side reinforced configuration develops lowest in-plane stresses.

In conclusion, these results suggest that the addition of an e-PTFE reinforcement material can affect the stresses, and therefore, the mechanical durability of the membrane. In particular, during asymmetric RH cycling, the residual in-plane tensile stresses, which can play a significant role in mechanical degradation and membrane lifetime, are lowered significantly for anode side reinforced configuration. Our numerical predictions therefore, can provide a basis for the design and optimization of composite PEM fuel cell membranes with the aim of reducing life-cycle cost by improving fatigue resistance.

## Acknowledgements

This research has been supported by DOE grant DE-FC36-086018052 through a subcontract from W. L. Gore & Associates, Inc.

## Appendix A. Strain formulations

### A.1. Swelling strains

The swelling strains in the reinforced membrane, caused by water uptake, are calculated using an empirical relationship based on volumetric swelling [43],

$$\varepsilon^S = \xi_i \left( \frac{\theta}{\theta_0} \right) \ln \left( \frac{1}{\phi_p} \right) \delta_{ij}, \quad (\text{A-1})$$

where  $\theta$  and  $\theta_0$  are the current and reference temperature (in K), respectively. The term  $\xi_i$  is the anisotropy ratio giving the dimensional change in the  $i$ -direction in the membrane relative to the total volume change of the membrane such that  $\xi_x + \xi_y + \xi_z = 1$ . The term  $\phi_p$  is the polymer volume fraction given by

$$\phi_p = \frac{EW/\rho_p}{18\lambda + EW/\rho_p}, \quad (\text{A-2})$$

where  $\lambda$  is the number of water molecules attached to each sulfonic acid group, EW is the equivalent weight of the ionomer (=1100) and  $\rho_p$  is the density of the dry ionomer material (=1970 kg m<sup>-3</sup>).

### A.2. Thermal strains

Assuming isotropic thermal expansion, the thermal strains in the membrane caused by a change in temperature ( $\theta - \theta_0$ ) are given by

$$\varepsilon_{ij}^T = \alpha(\theta - \theta_0)\delta_{ij}, \quad (\text{A-3})$$

where  $\alpha$  is the linear coefficient of thermal expansion and  $\delta_{ij}$  is the Kronecker delta given by

$$\delta_{ij} = \begin{cases} 1; & i = j \\ 0; & i \neq j \end{cases}. \quad (\text{A-4})$$

### A.3. Strain in the elastic–plastic (EP) layer

Extrapolating the spring concept in the elastic–plastic layer to represent a generalized three-dimensional isotropic Hooke's law response, the elastic strain can be written as a function of the stress in the elastic–plastic layer,  $\sigma_{ij}^{\text{EP}}$

$$\left( \varepsilon_{ij}^{\text{EP}} \right)_{\text{el}} = \frac{1 + \nu}{K_p} \sigma_{ij}^{\text{EP}} - \frac{\nu}{K_p} \delta_{ij} \sigma_{kk}^{\text{EP}}, \quad (\text{A-5})$$

where  $\nu$  is Poisson's ratio and  $K_p$  is the stiffness of the elastic element in this network.

Assuming isotropic strain hardening (represented by the spring,  $H$ , parallel to the slider element), the yield strength is a function of the plastic strain and temperature,  $\theta$ ,

$$\sigma_y = \sigma_y \left( \left( \bar{\varepsilon}_{ij}^{\text{EP}} \right)_{\text{pl}}, \theta \right). \quad (\text{A-6})$$

In this expression,  $\left( \bar{\varepsilon}_{ij}^{\text{EP}} \right)_{\text{pl}}$  is the equivalent plastic strain given by

$$\left( \bar{\varepsilon}_{ij}^{\text{EP}} \right)_{\text{pl}} = \int \sqrt{\frac{2}{3} d \left( \varepsilon_{ij}^{\text{EP}} \right)_{\text{pl}} d \left( \varepsilon_{ij}^{\text{EP}} \right)_{\text{pl}}}, \quad (\text{A-7})$$

where  $d \left( \varepsilon_{ij}^{\text{EP}} \right)_{\text{pl}}$  are the increments of plastic strain tensor.

Using von Mises' yield criterion [45], the rate-independent plastic flow is given by

$$f(\sigma_{ij}) = \sqrt{\frac{3}{2} S_{ij} S_{ij}} - \sigma_y, \quad (\text{A-8})$$

where  $\sigma_y$  is the yield strength of the material and  $S_{ij}$  are the deviatoric stress tensor components defined by

$$\epsilon_{ij} = \sigma_{ij} - \frac{1}{3} \sigma_{kk} \delta_{ij}. \quad (\text{A-9})$$

Under von Mises' yield criterion [45], the material deforms elastically for  $f(\sigma_{ij}) < 0$  and yielding occurs when

$$f(\sigma_{ij}, \epsilon_{ij}^{\text{pl}}) \geq 0. \quad (\text{A-10})$$

#### A.4. Strain in the first elastic–viscous ( $EV_1$ ) network

The total strain in the elastic–viscous network ( $EV_1$ ) is the sum of linear-elastic strain in the spring  $K_{EV_1}$  and the viscous strain in the dashpot element given by

$$\epsilon_{ij}^{EV_1} = (\epsilon_{ij}^{EV_1})_{\text{el}} + (\epsilon_{ij}^{EV_1})_{\text{vi}}, \quad (\text{A-11})$$

where the subscript el refers to the elastic portion and vi refers to the viscous portion of the strain. Assuming isotropic Hooke's law for the linear-elastic constitutive response of the spring in this network, the generalized, three-dimensional elastic strain as a function of the stress  $\sigma_{ij}^{EV_1}$ , is given by

$$(\epsilon_{ij}^{EV_1})_{\text{el}} = \frac{1+\nu}{K_{EV_1}} \sigma_{ij}^{EV_1} - \frac{\nu}{K_{EV_1}} \delta_{ij} \sigma_{kk}^{EV_1}. \quad (\text{A-12})$$

For the dashpot element, the Norton-Hoff stress-strain rate law [46] is used, the generalized three-dimensional time-dependent form of which is written as

$$\dot{\epsilon}_{ij}^{\text{vi}} = A (\sigma_{ij}^{\text{vi}})^n, \quad (\text{A-13})$$

where  $A$  and  $n$  are material parameters.

## References

- [1] B. Bahar, A.R. Hobson, J.A. Kolde, in: U.S. Patent (Ed.), U.S., 1997.
- [2] B. Bahar, A.R. Hobson, J.A. Kolde, D. Zuckerbrod, in: U.S. Patent (Ed.), U.S., 1996.
- [3] F. Liu, B. Yi, D. Xing, J. Yu, H. Zhang, *Journal of Membrane Science* 212 (2003) 213–223.
- [4] K.M. Nouel, P.S. Fedkiw, *Electrochimica Acta* 43 (1998) 2381–2387.
- [5] T.L. Yu, H.-L. Lin, K.-S. Shen, L.-N. Huang, Y.-C. Chang, G.-B. Jung, J.C. Huang, *Journal of Polymer Research* 11 (2004) 217–224.
- [6] Y.-H. Liu, B. Yi, Z.-G. Shao, D. Xing, H. Zhang, *Electrochemical and Solid-state Letters* 9 (2006) A356–A359.
- [7] M.B. Satterfield, P.W. Majsztrik, H. Ota, J.B. Benziger, A.B. Bocarsly, *Journal of Polymer Science Part B-polymer Physics* 44 (2006) 2327–2345.
- [8] M.L. Hill, Y.S. Kim, B.R. Einsla, J.E. McGrath, *Journal of Membrane Science* 283 (2006) 102–108.
- [9] M.H. Woo, O. Kwon, S.H. Choi, M.Z. Hong, H.-W. Ha, K. Kim, *Electrochimica Acta* 51 (2006) 6051–6059.
- [10] C. Yang, P. Costamagna, S. Srinivasan, J. Benziger, A.B. Bocarsly, *Journal of Power Sources* 103 (2001) 1–9.
- [11] C. Yang, S. Srinivasan, A.B. Bocarsly, S. Tulyani, J.B. Benziger, *Journal of Membrane Science* 237 (2004) 145–161.
- [12] Y.S. Kim, F. Wang, M. Hickner, T.A. Zawodzinski, J.E. McGrath, *Journal of Membrane Science* 212 (2003) 263–282.
- [13] E. Chalkova, M.V. Fedkin, D.J. Wesolowski, S.N. Lvov, *Journal of the Electrochemical Society* 152 (2005) A1742–A1747.
- [14] S.J.C. Cleghorn, D.K. Mayfield, D.A. Moore, J.C. Moore, G. Rusch, T.W. Sherman, N.T. Sisofo, U. Beuscher, *Journal of Power Sources* 158 (2006) 446–454.
- [15] H.L. Tang, M. Pan, F. Wang, *Journal of Applied Polymer Science* 109 (2008) 2671–2678.
- [16] K. Patankar, D. Dillard, S. Case, M. Ellis, Y.-H. Lai, M. Budinski, C. Gittleman, *Mechanics of Time-dependent Materials* 12 (2008) 221–236.
- [17] J.R. Grohs, Y.Q. Li, D.A. Dillard, S.W. Case, M.W. Ellis, Y.H. Lai, C.S. Gittleman, *Journal of Power Sources* 195 (2010) 527–531.
- [18] Y.Q. Li, D.A. Dillard, S.W. Case, M.W. Ellis, Y.H. Lai, C.S. Gittleman, D.P. Miller, *Journal of Power Sources* 194 (2009) 873–879.
- [19] S. Stucki, G.G. Scherer, S. Schlagowski, E. Fischer, *Journal of Applied Electrochemistry* 28 (1998) 1041–1049.
- [20] R. Borup, J. Meyers, B. Pivovar, Y.S. Kim, R. Mukundan, N. Garland, D. Myers, M. Wilson, F. Garzon, D. Wood, P. Zelenay, K. More, K. Stroh, T. Zawodzinski, J. Boncella, J.E. McGrath, M. Inaba, K. Miyatake, M. Hori, K. Ota, Z. Ogumi, S. Miyata, A. Nishikata, Z. Siroma, Y. Uchimoto, K. Yasuda, K.I. Kimijima, N. Iwashita, *Chemical Reviews* 107 (2007) 3904–3951.
- [21] R. Borup, J. Davey, D. Wood, F. Garzon, M. Inbody, D. Guidr, DoE Hydrogen Program Review, 2005.
- [22] Y.H. Lai, C.K. Mittelsteadt, C.S. Gittleman, D.A. Dillard, *Journal of Fuel Cell Science and Technology* 6 (2009) 13.
- [23] J. Wu, X.Z. Yuan, J.J. Martin, H. Wang, J. Zhang, J. Shen, S. Wu, W. Merida, *Journal of Power Sources* 184 (2008) 104–119.
- [24] Y.L. Tang, A. Kusoglu, A.M. Karlsson, M.H. Santare, S. Cleghorn, W.B. Johnson, *Journal of Power Sources* 175 (2008) 817–825.
- [25] A. Kusoglu, A.M. Karlsson, M.H. Santare, S. Cleghorn, W.B. Johnson, *Journal of Power Sources* 161 (2006) 987–996.
- [26] C.S. Gittleman, F.D. Coms, Y.-H. Lai, *Membrane durability: physical and chemical degradation*, in: M. Mench, E.C. Kumbar, T.N. Veziroglu (Eds.), *Modern Topics in Polymer Electrolyte Fuel Cell Degradation*, Elsevier, 2011, pp. 15–88.
- [27] N.L. Garland, T.G. Benjamin, J.P. Kopasz, *ECS Transactions* 11 (2007) 923–931.
- [28] W. Liu, S. Cleghorn, *ECS Transactions* (2006) 263–273.
- [29] M.F. Mathias, R. Makharia, H.A. Gasteiger, J.J. Conley, T.J. Fuller, C.S. Gittleman, S.S. Kocha, D.P. Miller, C.K. Mittelsteadt, T. Xie, S.G. Yan, P.T. Yu, *Interface* (2005) 24–35.
- [30] U.S. DOE. [http://www1.eere.energy.gov/hydrogenandfuelcells/fuelcells/pdfs/component\\_durability\\_profile.pdf](http://www1.eere.energy.gov/hydrogenandfuelcells/fuelcells/pdfs/component_durability_profile.pdf), 2007.
- [31] W. Liu, K. Ruth, G. Rusch, *Journal of New Materials for Electrochemical Systems* 4 (2001) 227–232.
- [32] N.S. Khattra, A.M. Karlsson, M.H. Santare, P. Walsh, F.C. Busby, *Journal of Power Sources* 214 (2012) 365–376.
- [33] Z. Lu, M. Lugo, M.H. Santare, A.M. Karlsson, F.C. Busby, P. Walsh, *Journal of Power Sources* 214 (2012) 130–136.
- [34] N.S. Khattra, in: Ph.D. Thesis, Mechanical Engineering, University of Delaware, Newark, DE, 2012.
- [35] A. Kusoglu, A.M. Karlsson, M.H. Santare, S. Cleghorn, W.B. Johnson, *Journal of Power Sources* 170 (2007) 345–358.
- [36] Y.L. Tang, A.M. Karlsson, M.H. Santare, M. Gilbert, S. Cleghorn, W.B. Johnson, *Materials Science and Engineering A-Structural Materials Properties Microstructure and Processing* 425 (2006) 297–304.
- [37] L.R.G. Treloar, *Proc Phys Soc* 60 (1948) 135–144.
- [38] R. Hill, *Series A. Mathematical and Physical Sciences* 193 (1948) 281–297.
- [39] ABAQUS, ABAQUS Inc, 2009.
- [40] Y.L. Tang, M.H. Santare, A.M. Karlsson, S. Cleghorn, W.B. Johnson, *Journal of Fuel Cell Science and Technology* 3 (2006) 119–124.
- [41] M. Griffith, T. Schmiedel, in: ECS Meeting, Honolulu, 2008.
- [42] F.N. Buchi, G.G. Scherer, *Journal of the Electrochemical Society* 148 (2001) A183–A188.
- [43] A. Kusoglu, M.H. Santare, A.M. Karlsson, S. Cleghorn, W.B. Johnson, *Journal of the Electrochemical Society* 157 (2010) B705–B713.
- [44] A. Kusoglu, Y.L. Tang, M.H. Santare, A.M. Karlsson, S. Cleghorn, W.B. Johnson, *Journal of Fuel Cell Science and Technology* 6 (2009).
- [45] R. von Mises, *Göttinger Nachrichten* 1 (1913) 582–592.
- [46] F.H. Norton, *Creep of Steel at Higher Temperatures*, McGraw-Hill Book Co, New York, 1929.
- [47] Z. Lu, in: Ph.D. Thesis, Mechanical Engineering, University of Delaware, 2012.
- [48] Z.W. Lu, C. Kim, A.M. Karlsson, J.C. Cross, M.H. Santare, *Journal of Power Sources* 196 (2011) 4646–4654.